Topology Driven g-Factor Tuning in Type-II Quantum Dots

J.M. Llorens,[1] V. Lopes-Oliveira,[2] V. López-Richard,[3] E.R. Cardozo de Oliveira,[3] L. Wewiór,[1]
J.M. Ulloa,[4] M.D. Teodoro,[3] G.E. Marques,[3] A. García-Cristóbal,[5] G.-Q. Hai,[6] and B. Alén[1,*]

[1] *Instituto de Micro y Nanotecnología, IMN-CNM, CSIC (CEI UAM+CSIC), Isaac Newton, 8, Tres Cantos, Madrid E-28760, Spain*
[2] *Universidade Estadual de Mato Grosso do Sul, Dourados, Mato Grosso do Sul 79804-970, Brazil*
[3] *Departamento de Física, Universidade Federal de São Carlos, São Carlos, São Paulo 13565-905, Brazil*
[4] *Institute for Systems based on Optoelectronics and Microtechnology (ISOM),Universidad Politécnica de Madrid, Ciudad Universitaria s/n, Madrid 28040, Spain*
[5] *Instituto de Ciencia de Materiales (ICMUV), Universidad de Valencia, Paterna E-46980, Spain*
[6] *Instituto de Física de São Carlos, Universidade de São Paulo, São Carlos, São Paulo 13560-970, Brazil*

(Received 17 September 2018; revised manuscript received 15 January 2019; published 4 April 2019)

We investigate how the voltage control of the exciton lateral dipole moment induces a transition from singly to doubly connected topology in type-II InAs/GaAs$_x$Sb$_{1-x}$ quantum dots. The latter causes visible Aharonov-Bohm oscillations and a change of the exciton g factor, which are modulated by the applied bias. The results are explained in the frame of realistic $\vec{k}\cdot\vec{p}$ and effective Hamiltonian models and could open a venue for new spin quantum memories beyond the InAs/GaAs realm.

DOI: 10.1103/PhysRevApplied.11.044011

I. INTRODUCTION

III-V semiconductor quantum dots (QDs) are a fundamental resource for quantum optical information technologies, from integrated quantum light sources to quantum optical processors [1]. Within this broad field, most knowledge arises from the InAs/GaAs system, with many other compounds being still relatively unexplored. III-Sb QDs and rings are a good example. They can be grown by several epitaxial methods and can strongly emit in all the relevant telecom bands, yet, III-Sb infrared quantum light sources are to be developed. III-Sb compounds also have the largest g factor and spin-orbit coupling (SOC) constant of all semiconductors but, with the exception of InSb nanowires, [2] this advantage has yet to be exploited in spin-based quantum-information technologies. One advantage of III-V-based quantum nanostructures is that optical initialization and readout can be done in a few nanoseconds using, for instance, the singly charged exciton lambda system with electrons [3] or holes [4]. Using the hole brings the additional benefit of its p-orbital character, meaning that the overlap between the atomic orbitals and the nucleus is significantly smaller than for the s-like electrons, diminishing the decoherence caused by the hyperfine interaction [4,5].

For quantum-information processing in the solid state, the possibility to modify the g factor through an external bias is its most outstanding resource [6]. Thanks to spin-orbit coupling terms in the Hamiltonian, the application of an electric field can modify the g-factor magnitude and sign through changes in the orbital part of the QD wave functions [7–9]. A similar effect can be obtained changing the elastic strain around the QD [10]. Since the g factor and wave functions are anisotropic, the observed modulation is different in Faraday [11–14] and Voigt [15] configurations. With InAs/GaAs QDs, external bias in the range of tens of kV cm^{-1} is necessary and, to prevent electron tunneling out of the QD, the introduction of blocking barriers is advisable [16,17]. Alternatively, one could use semiconductor nanostructures with larger spin-orbit coupling constants to produce larger modulations at lower bias.

Meanwhile, quantum nanostructures with a ring-shaped topology for electrons, holes or both and type-I or type-II confinement have been the object of intense theoretical and experimental research [18–28]. When two particles travel around these quantum rings (QR) circumventing a magnetic flux, the Aharonov-Bohm (AB) effect changes the relative phase factor of their wave functions [29]. The optical Aharonov-Bohm effect (OABE) can be detected at optical frequencies through the relative changes in the electron and hole orbital angular momenta. At zero magnetic field, electron-hole exchange interaction typically leads to a dark ground state doublet split by a few hundred μeV from the bright exciton doublet. With increasing applied magnetic field, higher-energy states with nonzero orbital angular momentum cross this quadruplet becoming the

---

[*] benito.alen@csic.es

new ground state of the system. These states are hence optically forbidden and must produce a fadeout of the emitted intensity. [30] In actual samples, such a reduction on the emitted light is not observed because of the reduced symmetry of the system, i.e., the orbital angular momentum is not a good quantum number any longer. As a consequence, oscillations in energy and intensity are observed instead of a quench [30]. The evolution of charged excitons becomes more complex in either case [31–33].

Given the different orbital confinement found in singly and doubly connected potentials, nanostructures with electrically tunable topology might be of great interest to couple spin and orbital degrees of freedom [33,34]. In the following, we investigate such a possibility, focusing on type-II InAs/GaAs$_x$Sb$_{1-x}$ QDs grown on GaAs and embedded in a p-i-n diode structure. For Sb molar fractions beyond 16%, the band alignment changes from type I to type II, with the electron confined inside the InAs and the hole delocalized in the GaAs$_x$Sb$_{1-x}$ overlayer [35–37]. The resulting wave-function configuration brings two important assets. Firstly, the weak localization of the hole results in a larger exciton polarizability or, in other words, a higher tunability of the exciton energy. Voltage control of the exciton dipole moment in the vertical direction thus allows large tuning of the radiative lifetime [34,38]. Secondly, we see that, pushing or pulling the hole against the bounding interfaces of the overlayer, also brings a topological change in the hole ground-state wave function as schematically shown in Fig. 1. By this manipulation, we are in fact engineering the wave-function density of probability from dot to ringlike as originally discussed in Ref. [23].

The rest of the paper is organized as follows. The details of the sample and optical characterization are summarized in Sec. II. We present in Sec. III the magneto-optical photoluminescence results. We first find that both, the diamagnetic coefficient and the g factor, can be modulated by the applied bias. Then, we report oscillations of the emission intensity and the degree of circular polarization (DCP) with the applied magnetic field, which occur only under forward bias. We discuss these effects in Sec. IV, relying on two different theoretical models. The first one is described in Sec. IV A. It consists of a multiband $\vec{k}\cdot\vec{p}$ axisymmetric model, which provides a quantitative evolution of the orbital-related effects: the diamagnetic coefficient dependence and the intensity oscillation. The limitation of the axial symmetry of this model is complemented with an effective mass model in Sec. IV B. It is based on a parabolic confinement, which can analytically evolve from a dotlike to a ringlike potential and includes an eccentricity parameter. From the solutions of this model, we discuss the spin-related results (g factor and DCP) in Sec. IV C by including the Rashba contribution in the Hamiltonian.

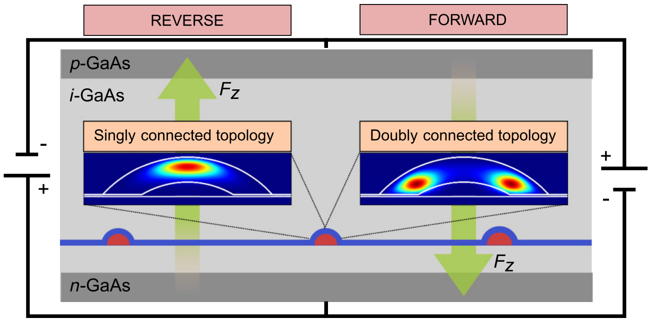

FIG. 1. Depiction of the p-i-n diode operational principle acting on the hole wave function. Depending on the polarization of bias the applied electric field (F_z) points upwards (left) or downwards (right) changing the topology of the wave function from singly connected to doubly connected. The size of the elements is not to scale.

II. EXPERIMENTAL DETAILS

A. Sample and device

A p-i-n diode is grown by MBE on a n-type GaAs (001) substrate. The intrinsic GaAs region spans 400 nm embedding in its center a single layer of self-assembled InAs QDs. After the formation of the QDs, they are covered by a 6-nm-thick GaAs$_x$Sb$_{1-x}$ layer with 28% nominal content of Sb. More details about the growth recipe and the morphological changes induced by rapid-thermal-annealing (RTA) treatment of these QDs can be found elsewhere [40]. After the RTA treatment, mesas of different sizes and ohmic contacts are defined by conventional optical-lithography techniques.

B. Optical characterization

To investigate OABE in our sample, magnetophotoluminescence (MPL) spectra are recorded at 5 K in the Faraday configuration up to 9 T. To avoid unnecessary manipulations, the light polarization is analyzed in the circular basis reversing the magnetic field direction. After the circular polarization analyzer, the emission is coupled into a multimode optical fiber and then imaged into the 100-μm-wide slits of a 300-mm focal length monochromator (1200 lines/mm grating). The light intensity is measured with a peltier cooled In$_x$Ga$_{1-x}$As photomultiplier connected to a lock-in amplifier. For every magnetic field, a PL spectrum is recorded for V(V) $= -2, -1, 0, 1$, and 1.35 (corresponding to 88, 63, 38, 13, and 4.2 kV cm^{-1}, respectively). $V < 0$ (> 0) corresponds to reverse (forward) bias as indicated in Fig. 1. The power of the temperature-stabilized 690-nm diode laser is registered simultaneously with its value constant within ±4% during the whole experiment and within ±0.2% while scanning the voltage at fixed magnetic field. Each spectrum is normalized by its corresponding excitation power and then analyzed by Gaussian deconvolution.

III. BIAS-DEPENDENT MAGNETOPHOTOLUMINESCENCE EXPERIMENTS

Figures 2(a)–2(e) show the evolution of the σ^--polarized MPL spectra in vertical electrical fields (F_z) between 88 and 4.2 kV cm^{-1}. To highlight the magnetic field effects, the lower panels of Fig. 2 show the evolution after subtraction and normalization by the spectrum at 0 T. In our previous work, we investigated the electric field response at 0 T of the type-II InAs/GaAs$_x$Sb$_{1-x}$ QD system [34]. A large reverse bias increases the electron tunneling rate out of the InAs quantum-dot potential towards the GaAs barrier. This leads to a noticeable intensity quenching moving to the left in the upper panel of Fig. 2. The electric field also reduces the electron-hole overlap and red shifts the peak emission energy at 0 T. In the following, we focus on the changes produced by F_z in the magnetic response of the sample. To maintain a unified description, the excitation conditions are kept approximately the same in the experiments of Ref. [34] and here. Thus, the PL emission comprises two bands, which are split by approximately 36 meV at 0 V and 0 T. These bands arise from the ground state and bright excited-state recombinations, both inhomogeneously broadened. Their integrated intensity ratio varies with F_z and is always larger than seven.

The magnetic properties are discussed attending solely to the evolution of the PL near the ground state of the system. For every F_z, the σ^+ and σ^- MPL spectra are recorded up to 9 T. Gaussian deconvolution is then applied to extract the overall evolution of the ground-state emission. From the deconvoluted MPL peak energy, E_σ, and integrated intensity, I_σ, we obtain the average energy shift, $E_\alpha = (E_{\sigma^+} + E_{\sigma^-})/2$, unpolarized integrated intensity, $I = (I_{\sigma^+} + I_{\sigma^-})/2$, Zeeman splitting, $\Delta E_z = E_{\sigma^+} - E_{\sigma^-}$, and degree of circular polarization, $\mathrm{DCP} = (I_{\sigma^+} - I_{\sigma^-})/(I_{\sigma^+} + I_{\sigma^-})$ for the low-energy band alone.

Figure 3 gathers the diamagnetic energy shift $\Delta E_\alpha = E_\alpha(B) - E(0)$ and Zeeman splitting for different electric fields. Solid lines are quadratic and linear fittings to $\Delta E_\alpha(B) = \alpha_D B^2$ and $\Delta E_z(B) = \mu_B g B$, respectively, where μ_B is the Bohr magneton, and α_D and g represent

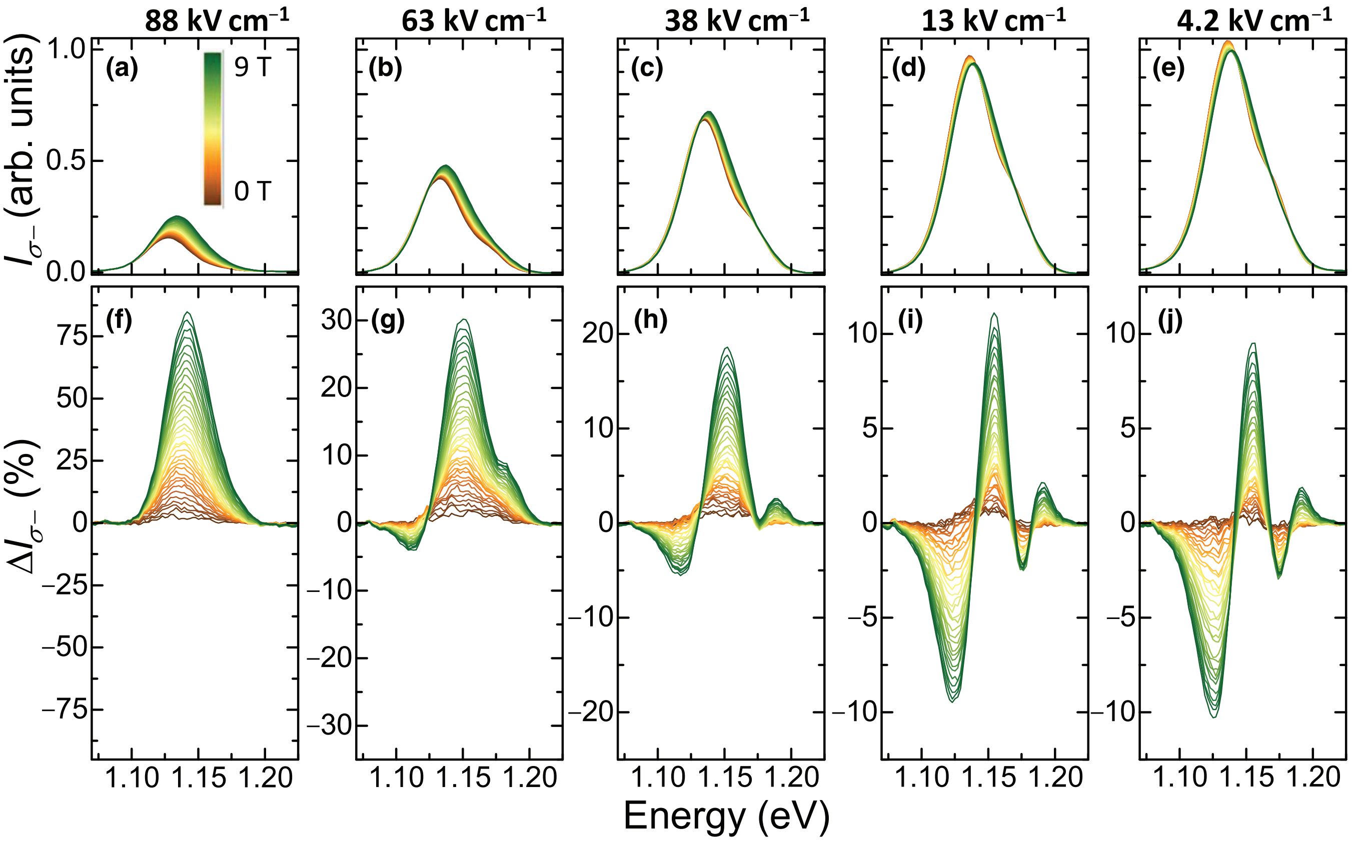

FIG. 2. (a)–(e) Evolution of the σ^--polarized magnetophotoluminescence in vertical electrical fields between 88 and 4.2 kV cm^{-1}. To highlight the magnetic field effects, (f)–(j) show the evolution after subtraction and normalization by the spectrum at 0 T. Corresponding figures for σ^+ detection and details about the Gaussian deconvolution procedure are given in Ref. [39].

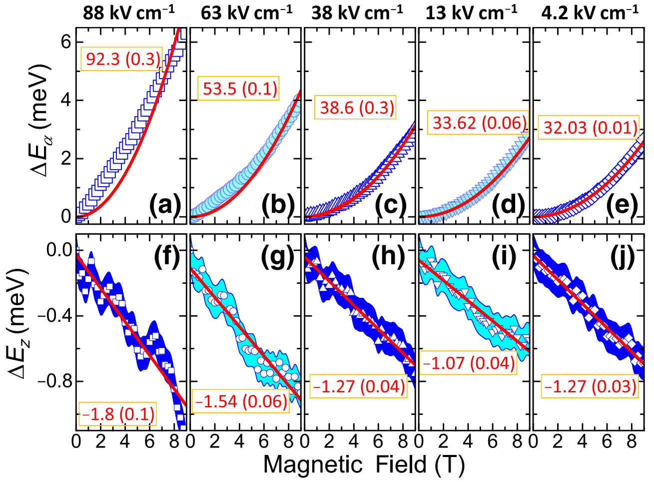

FIG. 3. (a)–(e) Dependence of the diamagnetic shift on the applied electric field. Solid lines stand for parabolic fits obtained with the indicated diamagnetic shift coefficients, α_D. (f)–(j) Experimental Zeeman splittings (symbols) and corresponding g factors extracted from their linear dependence (solid lines). Shaded areas correspond to the standard errors arising from Gaussian deconvolution of the emission band.

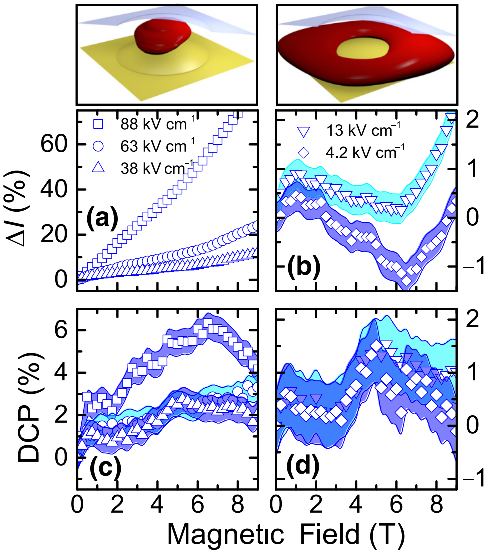

FIG. 4. Evolution of the unpolarized integrated intensity and degree of circular polarization in the high (a),(c) and low (b),(d) bias regime. Top panels represent the qualitative evolution of the hole probability density between both regimes. Shaded areas correspond to the standard errors arising from Gaussian deconvolution of the emission band.

the diamagnetic shift coefficient and Landé g factor for the type-II exciton, respectively [41]. Both functions describe accurately the data, except for a linear deviation for ΔE_α in the strong tunneling regime corresponding to relatively large electric fields in Figs. 3(a) and 3(b). We observe that both α_D and g are affected by the external electric field and also that oscillations in magnetic field are absent for the ground-state peak energy. In this bias range, the g-factor variation is approximately 80% and is attributed to a voltage modulation of the spin-orbit interaction, as discussed in detail in Sec. IV C.

The α_D variation is even more pronounced and exhibits a clear diminishing trend reducing the reverse bias. For a magnetic field applied in the growth direction, the diamagnetic shift is usually associated with the exciton wavefunction extension in the growth plane [42]. However, this simple correlation between exciton diameter and diamagnetic shift magnitude is lost when electronic levels with different angular momentum cross each other in the fundamental state. These level crossings are the source of the interference between different quantum paths leading to AB magneto-oscillations in quantum rings [18]. In an ensemble experiment, they might be obscured by inhomogeneous effect but might reveal themselves as a flattening of $\Delta E_\alpha(B)$ and the observed evolution of α_D vs F_z. In our case, the tunneling also becomes more important as the positive field increases. In these conditions, the electron wave function penetrates in the barrier and might also affect the value of α_D. These issues are discussed in detail in the next sections.

The evolution of the unpolarized integrated intensity after subtraction and normalization by the 0-T value, ΔI, and the DCP are depicted in Fig. 4. At large electric fields, ΔI increases with B exhibiting a strong magnetic brightening up to 75% [Fig. 4(a)]. The dependence follows a fixed linear slope with small oscillations, which are only apparent in the first derivative of the data (not shown). By reducing F_z, the magnetic brightening effect diminishes and, below 13 kV cm^{-1}, an oscillatory behavior develops [Fig. 4(b)]. In the same bias range, the DCP is positive, as expected from the negative g factor, and evolves with magnetic field from a rather monotonic dependence at 83 kV cm^{-1} to a clearly oscillatory one at 4.2 kV cm^{-1}.

IV. DISCUSSION

In the quantum-ring literature, MPL intensity oscillations are related to changes in the ground-state angular momentum arising from the OABE [18]. Voltage modulation of such oscillations have been reported for type-I InAs/GaAs single quantum rings [43,44], and also predicted for 2D materials [45]. The modulation must be associated to changes in the effective quantum-ring confinement potential. In the type-II InAs/GaAs$_x$Sb$_{1-x}$ QD system, holes are spatially localized within the GaAs$_x$Sb$_{1-x}$ layer near the InAs QDs [34,37,46–49]. The strain distribution and electron-hole Coulomb interaction create a net attractive potential for the hole that is balanced by the InAs/GaAs$_x$Sb$_{1-x}$ and GaAs/GaAs$_x$Sb$_{1-x}$ valence-band offsets. An external electric field modulates the geometry of this potential and, in turn, a change of the hole wave-function topology from singly to doubly connected is expected. The inset in Fig. 4 represents the qualitative evolution of the hole probability density according to the theoretical description developed in Ref. [34].

A. Axially symmetric $\vec{k} \cdot \vec{p}$ model

To analyze our data quantitatively, we start with an axially symmetric model for the type-II InAs/GaAs$_x$Sb$_{1-x}$ QD system. Under this approximation, the total angular momentum is a good quantum number for the exciton states and allows a proper labeling scheme. The whole $\vec{k} \cdot \vec{p}$ Hamiltonian including the strain is forced to be axially symmetric. Hence, even in the multiband case, the states are labeled according to the z projection of the total angular momentum (M). In the case of small band mixing, the state can also be labeled with the z projection of the orbital angular momentum of the envelope function associated with the main Bloch component (m). Further details and explicit expressions can be found in Appendix A.

The numerical results are obtained for a quantum dot of the same size and composition as those analyzed in our previous studies [34,40]. The geometry of the In$_x$Ga$_{1-x}$As QD is a lens shape of radius $R_{\mathrm{QD}} = 11$ nm and height $H_{\mathrm{QD}} = 3$ nm. It sits on top of a 0.5-nm In$_x$Ga$_{1-x}$As wetting layer (WL) and is surrounded by a GaAs$_x$Sb$_{1-x}$ shell of 6-nm thickness, which plays the role of the overlayer. The composition of the nanostructure is Ga$_{0.25}$In$_{0.75}$As and that of the overlayer GaAs$_{0.80}$Sb$_{0.20}$.

Figure 5 shows the results in the exciton picture. Each electron (hole) state is defined by the quantum number $M_{e(h)}$ introduced in Eq. (A2). Hence, the exciton states are defined by the addition of the total angular momentum of the constitutive particles $M = M_e + M_h$ (z projections). The only optically active exciton states are those characterized by $M = 0, \pm 1$. The emitted photons are polarized along the z direction for $M = 0$ and circularly polarized $\sigma_\pm$ for $M = \pm 1$. We have selected five values of the electric field, which fully cover the topological transition from dot to ring. For clarity, we have added a contour plot of the hole probability density on top of each energy-level dispersion. One can easily distinguish the localization of the hole particle on top of the nanostructure (115 kV cm^{-1}) and its drift towards the base as the electric field diminishes. The

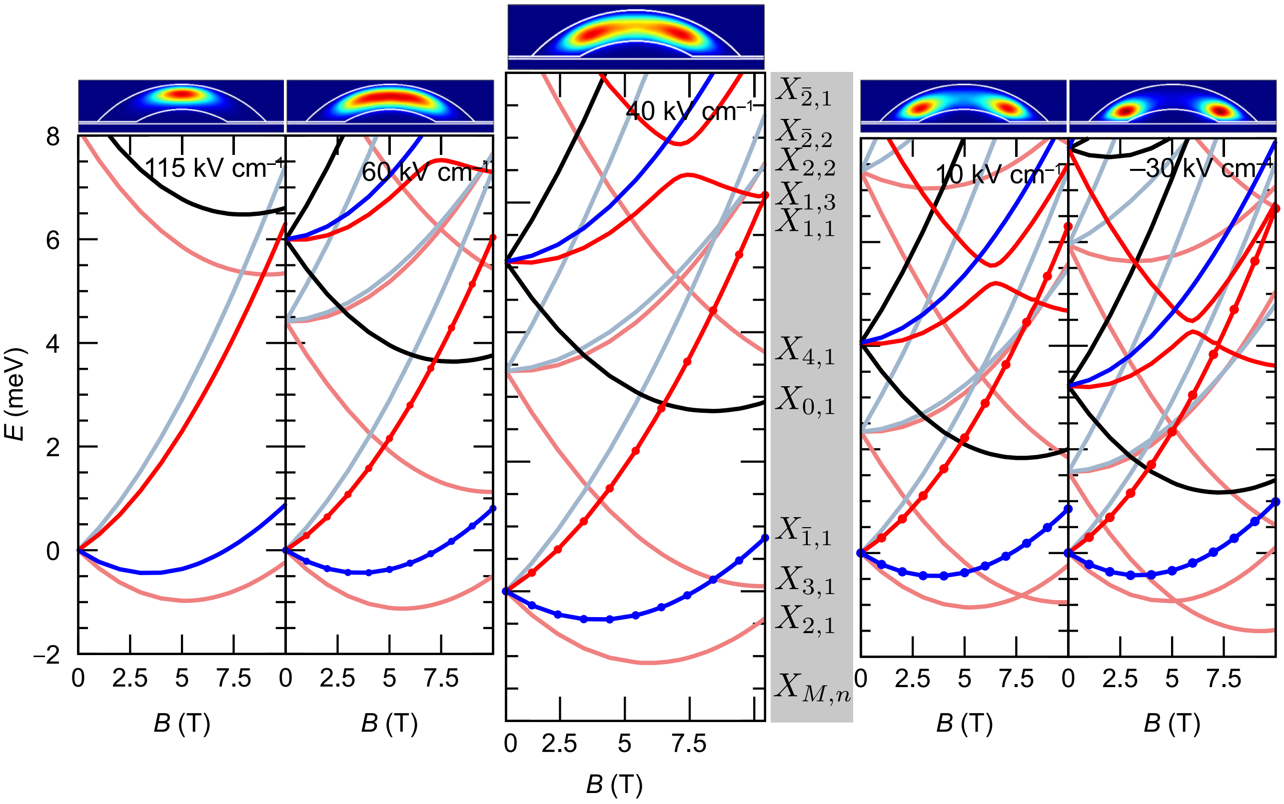

FIG. 5. Exciton energy levels relative to the ground-state energy at $B = 0$ T. Blue lines are states with $M = -1$, red lines $M = 1$, light-red lines $M > 1$, light-blue $M < -1$ and black $M = 0$. The spot size is proportional to the radiative rate and is brought to the same scale throughout the panels. The contour plot on top of each plot depicts the probability density of the hole ground state at $B = 0$ T. The axes dimensions are 50 and 12.5 nm.

corresponding exciton states are indicated only for the central panel as $X_{M,n}$, being $M = 0, \pm 1, \pm 2, \ldots$ the exciton total angular momentum z projection and $n = 1, 2, \ldots$ the principal quantum number of that particular M manifold. We first focus on the dispersion for $F_z = 115\,\mathrm{kV\,cm^{-1}}$ (large reverse bias). At $B = 0$ T, the ground state is composed of the fourth-fold degenerated quadruplet with $n = 1$ and $M = \pm 1$ and ± 2. The magnetic field splits this level into four branches. The $M = \pm 1$ can be distinguished by the nonzero radiative rate (dots over the line) and more intense colored lines used in the representation. These four exciton states result in the combination of two electron and two hole states whose dominant Bloch amplitudes are $|1/2, \pm 1/2\rangle$ and $|3/2, \pm 3/2\rangle$. The envelope function of each dominant Bloch amplitudes is defined by $m \approx 0$. This explains the weak dependence of the internal structure of the quadruplet to the electric field and hence to the topology of the hole wave function. Irrespective of whether the hole is located above the apex of the QD ($F = 115\,\mathrm{kV\,cm^{-1}}$) or close to its base ($F = -30\,\mathrm{kV\,cm^{-1}}$) the energy levels are weakly perturbed. In contrast, the quantization energy of the excited states is significantly perturbed by the electric field. The first excited state at $B = 0$ T is out of the plot for $F = 115$ kV cm^{-1}, while at $F = -30\,\mathrm{kV\,cm^{-1}}$ the energy splitting with the ground state is approximately 1.5 meV. This clearly illustrates how the electric field efficiently modifies the angular and radial confinement exerted on the hole wave function. In theses states, the dominant envelope wave functions of the hole is characterized by $|m| > 0$ and therefore are more sensitive to the vertical position within the overlayer.

Figure 5 illustrates that the applied electric field can effectively isolate the ground state from the excited states for $F > 60\,\mathrm{kV\,cm^{-1}}$ or bunch excited and ground states together for $F < 60\,\mathrm{kV\,cm^{-1}}$. In the bunching regime, the model predicts the crossing between states of different M, and thus a change in the ground-state orbital confinement. More explicitly, the $X_{3,1}$ high-energy state and the $X_{\bar{1},1}$ and $X_{2,1}$ low-energy states cross at $B = 5.4$ and 7.8 T for $F = 10\,\mathrm{kV\,cm^{-1}}$, respectively. These crossings occur at fields within the range of the experimental values presented before. This would result in the possibility of observing experimentally, at least, the crossing between $X_{3,1}$ and the states of lower energy and thus an associated optical AB oscillation. The precise correspondence with the experimental results is difficult to establish given that its observation would depend on the thermalization of the excited carriers and the eventual relaxation of the selection rules in the actual QDs, as explained below. As expected for AB-related effects, the number of crossings and their actual positions depend on the exciton in-plane dipole moment which, in our case, decreases with the electric field. In view of these results, the oscillatory dependence observed for the unpolarized integrated intensity and DCP in Fig. 4 is a consequence of a change in the total angular momentum of the ground state and hence a signature of the OABE.

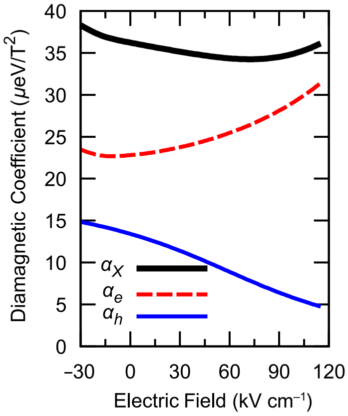

FIG. 6. Diamagnetic coefficient for the electron (dashed red line), hole (solid blue line), and the exciton (thick-solid black line) states.

The inhomogeneous broadening of the MPL spectra in Sec. III prevents the observation of the individual energy levels shown in Fig. 5, thus peak-energy magneto-oscillations cannot be detected in our experiment [28]. This notwithstanding, our analysis of the emission energy shifts in Figs. 3(a)–3(e) revealed a threefold increase of the diamagnetic shift coefficient with the electric field. From the numerical results shown in Fig. 5, we calculate this magnitude for the bright exciton states. The resulting coefficients for the electron α_e, hole α_h, and exciton α_X are shown independently in Fig. 6.

The hole diamagnetic shift decreases from approximately 15 to approximately $5\,\mu\mathrm{eV/T^2}$ by increasing the electric field from -30 to $115\,\mathrm{kV\,cm^{-1}}$. This is expected since, during the hole drift from the base towards the apex of the overlayer, its density of probability shrinks, decreasing α_h (see contour plot insets in Fig. 5) [42]. In the same bias range, α_e goes from approximately 23 to approximately $32\,\mu\mathrm{eV/T^2}$, increasing with the reverse bias. This is a consequence of the spillover of the electron wave function in the GaAs barrier underneath. For $F_z > 60\,\mathrm{kV\,cm^{-1}}$, electron tunneling out of the InAs QD becomes noticeable [34]. The numerical model catches this situation only approximately and, for the largest bias, the calculated α_X is only 37 $\mu\mathrm{eV/T^2}$, while experimentally α_D is $92.3\,\mu\mathrm{eV/T^2}$. Indeed, for $F_z > 63\,\mathrm{kV\,cm^{-1}}$, the experimental dispersion becomes increasingly linear. Linear dispersion is characteristic of the Landau regime. In our context, it corresponds to a weaker confinement as a result of the delocalization of the electron wave function as the tunnel regime becomes dominant [see Figs. 3(a) and 3(b)]. In the opposite bias regime, the correspondence with the experimental values is much better. α_D ($32.62\,\mu\mathrm{eV/T^2}$) is found at $F = 4.2\,\mathrm{kV\,cm^{-1}}$ while α_X renders 36.05 $\mu\mathrm{eV/T^2}$. As shown in Fig. 5, in this bias range, the ground state of the electron-hole system is composed mostly of states with angular momentum $|M| > 1$. Under the axially symmetric approximation, these states are purely dark and do not contribute to α_X. If the symmetry of the actual confinement potential is broken, they can achieve oscillator strength, lower further the diamagnetic shift, and explain the observed AB intensity oscillation, as discussed in the next section.

B. In-plane asymmetry effects

It has been profusely reported that quantum-dot elongation can take place after capping. The strain fields that build up during this process provoke the anisotropic segregation of In atoms leading to an eccentricity increase of previously cylindrical systems [50,51]. Analogous process is also triggered during the synthesis of type-II InAs/GaAs$_x$Sb$_{1-x}$ quantum dots, which also might lead to anisotropic piezoelectric fields [48,52]. Thus, it is a goal of our following discussion to assess the effects of in-plane confinement anisotropy in the electronic properties. To this end, we introduce an effective mass description of both the conduction and valence bands, and incorporate the effects of confinement asymmetry for electrons and holes in a model that can emulate quantum dots and rings within the same framework, as well as the resulting Rashba spin-orbit coupling fields arising from confinement and external fields.

The eigen-value problem for the conduction band is solved by expanding the corresponding wave functions in the basis of the eigensolutions of the following effective mass Hamiltonian,

$$H = \frac{\hbar^2}{2\mu^*}k^2 + V_0(z) + V_0(\rho) + \frac{g^*\mu_B}{2}\mathbf{B}\cdot\boldsymbol{\sigma}, \qquad (1)$$

with μ^* the effective mass, $\mathbf{k} = -i\nabla + e/\hbar\mathbf{A}$, and the magnetic field pointing along the growth z direction, where $\boldsymbol{\sigma}$ is the Pauli matrix vector, and $\mathbf{A} = B/2\rho\widehat{\varphi}$. For the unperturbed basis, $V(z)$ is assumed as a rigid wall potential profile while the in-plane confinement in polar coordinates takes the form [53]:

$$V_0(\rho) = \frac{a_1}{\rho^2} + a_2\rho^2 - 2\sqrt{a_1 a_2}, \qquad (2)$$

which allows an exact solution to be obtained that covers both the quantum-ring and the quantum-dot confinements. The parameters a_1 and a_2 define the structure shape and for $a_1 \neq 0$, a ring with radius $R_{\mathrm{QR}} = (a_1/a_2)^{1/4}$ is obtained. In turn, by setting $a_1 = 0$, a parabolic quantum dot with effective radius $R_{\mathrm{QD}}^2 = \hbar/(2\pi\sqrt{2a_2\mu^*})$ is emulated. This potential allows us to describe effectively the change of topology on the hole as a result of the applied electric field.

For the valence-band basis, used to expand the Luttinger Hamiltonian eigensolutions, we use an analogous separable problem yet assuming anisotropic effective masses in Eq. (1), and replacing $g^*/2$ and σ_z, by -2κ and the angular-momentum matrix for $j = 3/2$, J_z, respectively.

The symmetry constrains are subsequently relaxed by reshaping the in-plane confinement in the following way, $V(\rho,\varphi) = V_0(\rho) + \delta\cdot\rho^2\cos^2\varphi$. This is an extension of the profile proposed in Refs. [54,55], where the term controlled by the parameter δ determines the eccentricity of the outer rim of the confinement. The values of the eccentricity are given by $e = \sqrt{1 - a_2/(a_2+\delta)}$, for $\delta > 0$, that corresponds to an elliptical shrinking, or $e = \sqrt{1 - (a_2+\delta)/a_2}$ for $\delta < 0$, that leads to an elliptical stretching. Additionally, an electric field along the growth direction is considered by inserting the term eFz into $V(z)$ that couples the wave-function components of different parity. The details on the solution of the Schrödinger equation are in Appendix B. The asymmetric solution is given by the expansion

$$\Psi = \sum_{\alpha,n,m,l} C^{\alpha}_{n,m,l}\psi^{\alpha}_{n,m,l}(\rho,\varphi,z), \qquad (3)$$

where α labels the basis functions at the Brillouin-zone center in the Kane model ($|1/2,\pm 1/2\rangle$, $|3/2,\pm 3/2\rangle$, and $|3/2,\pm 1/2\rangle$), m is the z projection of the orbital angular momentum, n is the radial quantum number, and l is the vertical quantum number. Thus, the expansion coefficients, $C^{\alpha}_{n,m,l}$, determine the spin character of the final state, namely, the degree of hybridization of the various m components.

The eccentricity breaks the cylindrical symmetry. Figure 7(a) shows the impact of the symmetry break on the valence-band energy levels for the first few states confined in a QR with $R_{\mathrm{QR}} = 12$ nm, $a_2 = 0.05\ \mathrm{meV/nm^2}$ and height $h_{\mathrm{QR}} = 7$ nm. For this calculation, we omit the spin splitting. Dashed lines render the cylindrical case ($\delta = 0$ meV) mimicking the energy dispersion found in the previous section. Solid lines stand for an eccentric ring with $\delta = 2$ meV. The only relevant energy levels for the discussion are represented with bold lines and labeled as A, B, and C. The A and B levels cross at $B = 4$ T, and the A and C levels anticross at $B = 7.5$ T. The mixing of different m components reduces the effective diamagnetic shift of the valence-band ground hybrid state. This mixing is quantified in Fig. 7(b), where the expansion coefficients $\left|C^{\alpha}_{0,m,1}\right|^2$ resulting from the diagonalization of the valence-band Hamiltonian are depicted. In the symmetric case, the ground state experiences a sharp change at the crossing from a $m = 0$ character to a $m = 1$ (not shown). In contrast, in the eccentric case there are no discontinuities, reflecting a soft evolution of the wave-function character with the magnetic field. The states corresponding to the energy levels A and C swap their character from $m = 0$ to $m = 2$ at the anticrossing. The energy level B acquires a dominant $m = 1$ character being insensitive to the crossing and anticrossing.

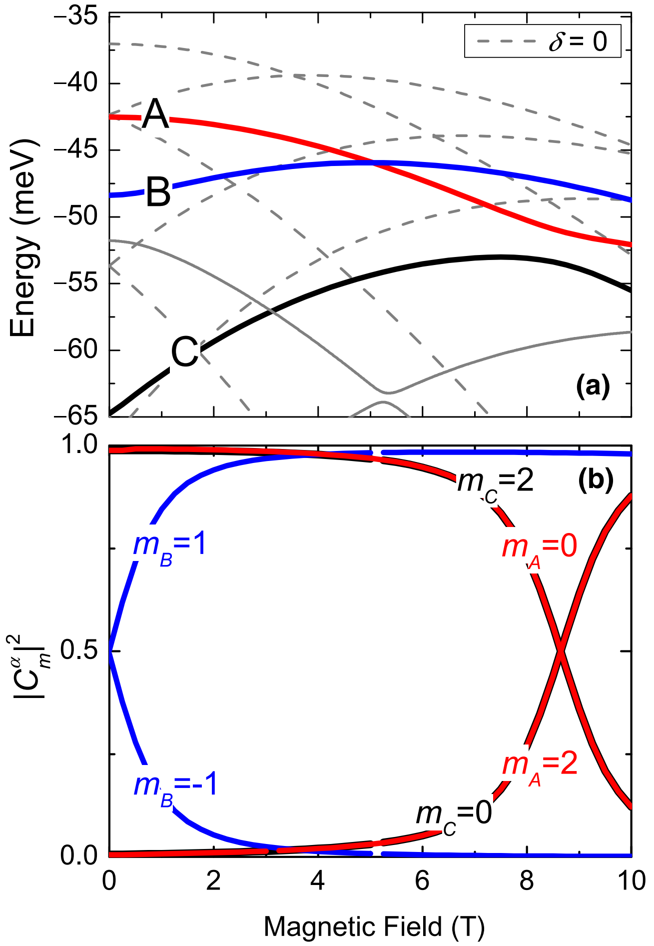

FIG. 7. (a) Calculated energy levels in a quantum ring for the top valence subband: solid curves correspond to an eccentric ring with $\delta = 2$ meV/100 nm^2 while the dashed curves are calculated for a cylindrical geometry with $\delta = 0$. (b) Calculated weight coefficients of the A, B, and C energy levels in (a) as a function of the magnetic field strength.

The changes of the electronic states' energy and character modulate also the emission intensity, which can be calculated from the oscillator strength (OS). As the electron ground state has $m = 0$ character, state B is optically inactive within the model, with its OS negligible. States A and C, however, show an exchange of oscillator strength as they approach the anticrossing as shown in Fig. 8. The smooth increase of the OS at high magnetic fields is attributed to the magnetic brightening. In this situation, we calculate the emission intensity of the system solving a simple rate equations model based on Ref. [56] as explained in Ref. [39]. The radiative rates are parameters of the model and scale with the OS calculated for states A and C. For state B, the pure dark condition is relaxed, since dark states must eventually recombine due to hybridization processes not considered here (e.g., electron-hole exchange). As shown in Fig. 8, our model predicts an intensity oscillation around 7 T with similar phase but slightly larger amplitude than the experimental evolution displayed in Fig. 4(b). It must be noted that the position of the crossings and the energy difference between states presents fluctuations among QDs. This shall lead to a shallower experimental oscillation resulting from the ensemble average of many curves like the ones shown in Fig. 8 [26].

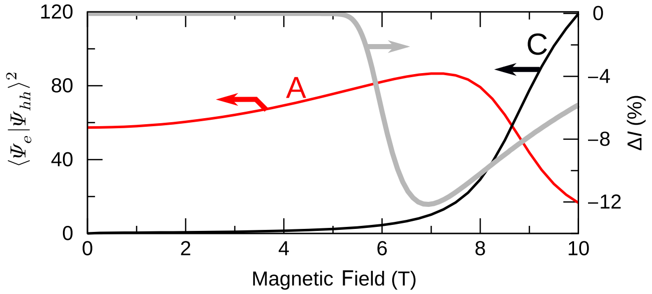

FIG. 8. Calculated oscillator strength for the interband transitions involving the conduction-band ground state and the admixed valence-band levels A and C (thin red and black lines, respectively). Computed relative intensity ΔI with a rate equations model (thick gray line). The electrons are calculated for a QD of $R_{\mathrm{QD}} = 15$ nm and $h_{\mathrm{QD}} = 7$ nm. The eccentricity is $e = 0.53$.

C. Spin-orbit coupling effects

We have just shown that the symmetry reduction in a quantum ring lowers the effective diamagnetic shift of the ground state as the angular-momentum states become intermixed. In turn, including spin-orbit interaction terms, the electrical modulation of the lateral and vertical confinement also changes the spin states [10–14,16,17,57]. According to the results presented in Figs. 3(f)–(j), the exciton energy spin splitting increases with the device reverse bias. Meanwhile, within the GaAs$_x$Sb$_{1-x}$ overlayer, the hole wave-function geometry and topology evolve. Both observations can be connected once the spin-orbit interaction is incorporated to the model represented by Eqs. (1)–(3). The interaction is introduced through the Rashba contribution to the total Hamiltonian $H_R^c = \alpha_c \boldsymbol{\sigma} \cdot (\nabla V \times \mathbf{k})$, for the conduction band, or $H_R^v = \alpha_v \mathbf{J} \cdot (\nabla V \times \mathbf{k})$, for the valence band. The expression for the spin-orbit Hamiltonian assuming the confinement profile that includes all the asymmetry terms and the resulting energy corrections are given in Appendix C.

In turn, we can separate the spin-orbit effects induced by confinement and asymmetry into first- or higher-order contributions. The latter ones are produced by the coupling of previously unperturbed levels and appear strongly when these levels approach inducing (or enhancing) anticrossings, mostly at higher fields. The first-order terms appear already at vanishing fields and may provoke, for instance, the tuning of the effective Landé factor. We focus the discussion on these ones.

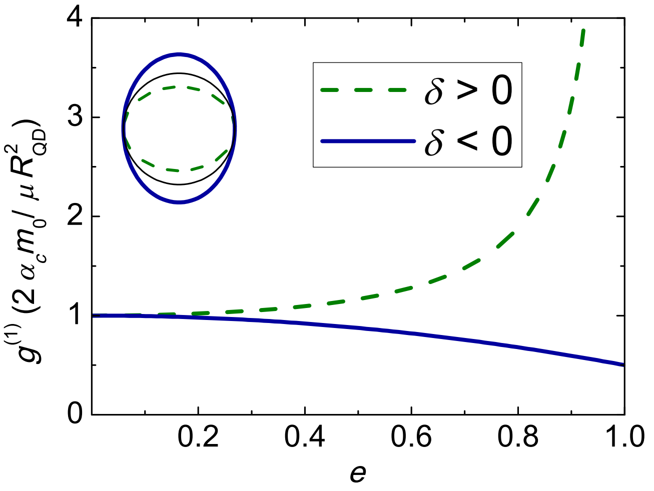

FIG. 9. Calculated first-order correction of the conduction-band g factor as a function of the eccentricity for a quantum dot according to Eq. (4).

The first-order correction to the conduction-band Zeeman splitting induced by the spin-orbit coupling can be calculated exactly for the ground state of a quantum dot according to [58]

$$g_c^{(1)} = \frac{2m_0\alpha_c}{\mu^* R_{\mathrm{QD}}^2}\left\{1+\mathrm{sign}(\delta)\frac{e^2}{2-[1+\mathrm{sign}(\delta)]\,e^2}\right\}. \qquad (4)$$

This result is depicted in Fig. 9 and illustrates how the g-factor correction grows as the quantum-dot volume is reduced by shortening R_{QD} or by shrinking the lateral confinement into an ellipse ($\delta > 0$ corresponds to an elliptical shrinking).

For a quantum ring, such a modulation is not trivial and depends on the way the confinement shape is modified as shown in Fig. 10. Note that by fixing a_2 and increasing a_1, the quantum-ring radius increases as a result of widening the inner rim [Fig. 10(a)]. Such a modulation of the confinement profile can either increase or decrease the valence-band g-factor correction according to the value of the eccentricity and the sign of δ as displayed in Fig. 10(b). For large enough rings, the eccentricity may even lead to an absolute reduction of the g factor. If in contrast, the parameter a_1 is fixed while increasing a_2, the confinement potential shrinks as a result of the reduction of the external radius. This condition is plotted in Fig. 10(c) while the corresponding first-order correction to the g factor appears in (d). Such a reduction of the quantum-ring radius provokes a monotonic increase of this correction factor regardless the value of the eccentricity.

Through this model, the nonmonotonic increase of the g factor displayed in Fig. 3 can be ascribed to the bias-dependent shrinkage and symmetry reduction of the hole wave function. To assess the absolute values of the g-factor correction, and the relevance of antimonides in that respect, we may contrast systems with different spin-orbit coupling: GaAs, GaSb, and InSb, respectively. For the valence band of these materials, $\alpha_v^{\mathrm{GaAs}} = -14.62\,\text{Å}^2$, $\alpha_v^{\mathrm{GaSb}} \approx 3.3\alpha_v^{\mathrm{GaAs}}$, $\alpha_v^{\mathrm{InSb}} \approx 38\alpha_v^{\mathrm{GaAs}}$. Their calculation is detailed in Appendix C. According to these values, the units used in Fig. 10 for the valence-band g-factor corrections are -0.012, for GaAs, -0.038, for GaSb, and -0.442, for InSb. In turn, for the conduction-band g-factor correction, plotted in Fig. 9 the units are radius dependent and for a pure InAs QD with $R_{\mathrm{QD}} = 8$ nm they equal 1.6.

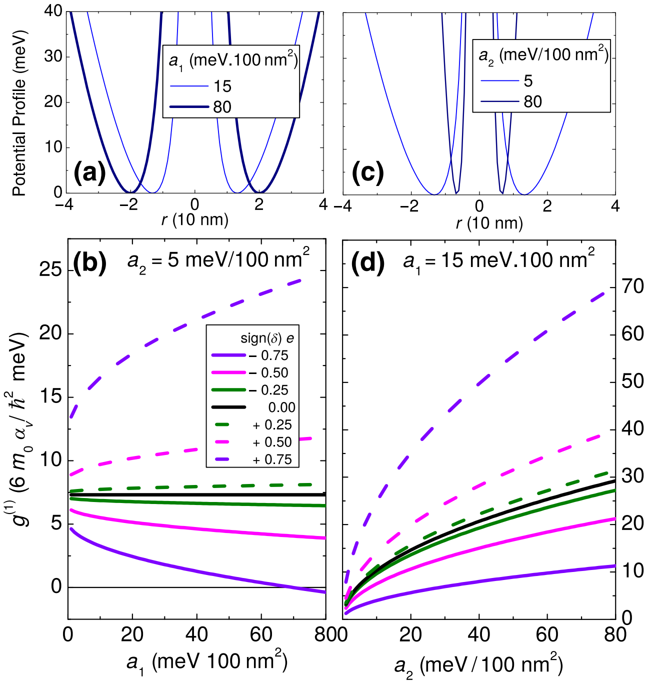

FIG. 10. (a) In-plane confinement profiles for fixed a_2 and varying a_1. (b) Calculated first-order correction of the g factor for fixed a_2 and varying eccentricity as a function of a_1. (c) In-plane confinement profiles for fixed a_1 and varying a_2. (d) Calculated first-order correction of the g factor for fixed a_1 and varying eccentricity as a function of a_2.

For electron-hole pairs confined in type-II nanostructures, the unperturbed effective Zeeman splitting can be obtained from $\Delta E_c^{(0)} - \Delta E_v^{(0)} = (g_c^0 + 6\kappa)\mu_B B$. In the case of an electron in InAs and a hole in GaAs$_{0.8}$Sb$_{0.2}$, the effective g factor is $g_{e-h}^{(0)} = g_c^{(0)}(\mathrm{InAs}) + 6\kappa(\mathrm{GaAs}_{0.8}\mathrm{Sb}_{0.2}) = -3.62$. By introducing the effects of confinement, the g factor can be corrected as $g_{e-h} = g_{e-h}^{(0)} + g_c^{(1)} - g_v^{(1)}$. Note that according to the values of $\alpha_c > 0$ and $\alpha_v < 0$, the correction leads to a g-factor increase in relative terms towards more positive values. For low fields, the electrons and holes are confined in QD shapes with $a_1 = 0$ and $a_2 = 5$ meV/100 nm^2 for holes while $R_{\mathrm{QD}} = 8$ nm for electrons. This leads to g-factor corrections of $g_c^{(1)} = 1.6$ and $g_v^{(1)} = 0.129$ for electrons and holes, respectively, leading to a total g factor $g_{e-h} =$

-1.891. At higher electric fields, the hole wave function moves downwards, where we can expect a radius increase of an eccentric QR ($R_{\mathrm{QR}}^2 = \sqrt{a_1/a_2}$) with $e = 0.53$. This translates into the model by a growing a_1 from 0 to 10 meV 100 nm^2, with $a_2 = 5$ meV/100 nm^2, corresponding to the QR with $R_{\mathrm{QR}} = 12$ nm characterized in Fig. 7. According to Fig. 10(b), this results in an increase on the correction of $g_v^{(1)} = 0.172$. In turn, the electron is confined inside of the QD and it could move upwards, with a smaller effective $R_{\mathrm{QD}} = 6.8$ nm with respect to the situation of larger positive fields. In Eq. (4), $g_c^{(1)}$ is inversely proportional to R_{QD} and therefore increases its value to $g_c^{(1)} = 2.21$. This translates into a total g factor of $g_{e-h} = -1.23$. The change in the estimation of the g factor between low and high fields agrees with the observed experimental evolution from -1.8 to -1.3.

V. CONCLUSIONS

In summary, we present experimental evidence on the tuning of the electronic structure of type-II InAs/GaAs$_x$Sb$_{1-x}$ quantum dots under vertical electric and magnetic fields. Induced by the external bias, the drift of the hole wave function in the soft confinement of the GaAs$_x$Sb$_{1-x}$ layer encompasses a wide range of geometrical and topological changes in the effective potential. These changes cannot be easily induced in type-I systems and provide a rich variety of insights on the way geometry affects the electronic structure and thus the optical response. The observed effects are studied with theoretical approaches that include electronic confinement, strain fields, and spin effects on the same footing. In particular, we report how the application of an external bias tunes the hole confinement geometry independently of the electron. Under certain bias conditions, the hole confinement topology changes and magnetic field oscillations are observed. The oscillations follow the orbital quantization of the hole state and are thus susceptible to the confinement size and eccentricity. Although further work is needed to put these ideas at work in single InAs/GaAs$_x$Sb$_{1-x}$ nanostructures, this modulation of hole orbital quantization, accompanied by the tuning of the exciton g factor, might pave the way for the voltage control of spin degrees of freedom as required by several quantum technologies.

ACKNOWLEDGMENTS

The authors gratefully acknowledge financial support from EURAMET through EMPIR program 17FUN06-SIQUST, from Spanish MINEICO through Grants No. TEC2015-64189-C3-2-R, No. MAT2016-77491-C2-1-R, No. EUIN2017-88844, and No. RYC-2017-21995, from Comunidad de Madrid through Grant No. P2018/EMT-4308, and from CSIC through Grants No. I-COOP-2017-COOPB20320 and No. PTI-001. Support from Brazilian agencies is also acknowledged through FAPESP Grant No. 2014/02112-3 and CNPq Grant No. 306414/2015-5.

APPENDIX A: DETAILS OF THE MULTIBAND AXISYMMETRIC MODEL

The electronic structure of the InAs/GaAs$_x$Sb$_{1-x}$ QDs is computed by the $\vec{k}\cdot\vec{p}$ method following Trebin *et al.*'s [59,60] notation. The final Hamiltonian is the result of adding three contribution, the $\vec{k}\cdot\vec{p}$ term ($H_{\vec{k}\cdot\vec{p}}$), the strain interactions (Bir-Pikus H_ε), and the magnetic interactions (H_B):

$$H = H_{\vec{k}\cdot\vec{p}} + H_\varepsilon + H_B. \tag{A1}$$

We neglect the linear k_i terms in the valence-valence interaction, the quadratic k_ik_j and ε_{ij} terms in the conduction-valence interaction, and the $k_i\varepsilon_{jk}$ in the strain-induced interactions. To simplify the analysis, we impose axial symmetry in all the terms involved in the Hamiltonian. This approximation also affects the strain distribution forcing us to consider the materials as elastically isotropic. Compact expressions are obtained with the Eshelby inclusions method [61] and Fourier transform of the strain tensor [62]. With this formalism we succeed in explaining Raman frequency shifts induced by the strain [63,64] and strain distributions extracted from middle-energy ion-scattering [65] experiments. The solution of the problem is obtained considering that only the band edges are discontinuous across material interfaces. To describe electrons and holes properly in type-II QDs, we decouple the conduction and valence bands in H. Hence, the electrons are described by a single band model, while a 6×6 Hamiltonian is used for the holes.

Axial symmetry allows us to define a total angular momentum of z component M, which is the result of adding the corresponding components of the envelope function orbital angular momentum (m) and Bloch's amplitude total angular momentum (j_z): $M = m + j_z$. Each electronic state is described by the wave function

$$\begin{aligned}\Psi^{(M)}(\vec{r}) &= \sum_{k=1}^{8} F_{m,k}^{(M)}(\vec{r})u_k \\ &= \sum_{k=1}^{8} \frac{1}{\sqrt{2\pi}} e^{im\phi}\mathcal{F}_{m,k}^{(M)}(\rho,z)u_k,\end{aligned} \tag{A2}$$

where u_k is the Bloch amplitude of the k band at the origin of the Brillouin zone and $F_{m,k}^{(M)}(\vec{r})$ is the envelope function associated to the k Bloch component. The envelope function in expressed cylindrical coordinates defined by a phase factor characterized by m and a two-dimensional component $\mathcal{F}_{m,k}^{(M)}(\rho,z)$.

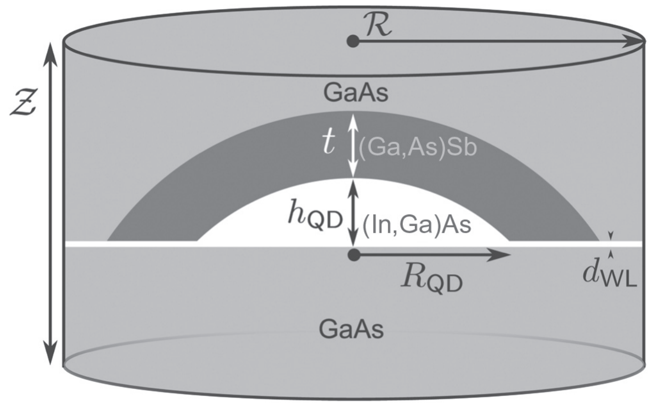

FIG. 11. Depiction of the geometrical model to describe a QD of radius $R_{\rm QD}$ and height $h_{\rm QD}$, a overlayer of thickness t and a wetting layer of thickness $d_{\rm WL}$ embedded in hard-wall cylinder of radius $\mathcal{R}$ and height $\mathcal{Z}$.

The solution of the Schrödinger equation is obtained by expanding Eq. (A2) in a complete basis. The basis is defined by the eigenfunctions of a hard-wall cylinder:

$$\mathcal{F}_{m,k}^{(M)} = \sum_{\alpha,\mu} \mathcal{N}_{\alpha}^{(m)} J_m \left[k_{\alpha}^{(m)} \rho/\mathcal{R}\right] \times \sqrt{2/\mathcal{Z}} \sin\left[\mu\pi \left(z/\mathcal{Z} - 1/2\right)\right], \tag{A3}$$

where $J_m(x)$ is the Bessel function of order m, $k_{\alpha}^{(m)}$ is its zero number $\alpha = 1, 2, \ldots$, $\mu = 1, 2, \ldots$, $\mathcal{R}$ and $\mathcal{Z}$ are the radius and height of the expansion cylinder and

$$N_{\alpha}^{(m)} = \frac{\sqrt{2}}{\mathcal{R}\left|J_{m+1}\left[k_{\alpha}^{(m)}\right]\right|} \tag{A4}$$

is the normalization of the radial part. This definitions ensure the orthonormality of the expansion basis. A similar procedure was followed by Tadic *et al.* in Refs. [66,67]. Further details can be found in Ref. [68].

In Fig. 11, we show an outline of the QD embedded in the overlayer enclosed by the expansion cylinder. The number of geometrical parameters is therefore reduced to six.

APPENDIX B: DETAILS OF THE EMA NONAXISYMMETRIC MODEL

The solution for the 3D Schrödinger equation, $\Phi(\rho, \theta, z)$, corresponding to the potential profile in Eq. (2) is given by

$$\psi_{n,m,l}^{(e/h)}(\rho, \varphi, z) = \phi_{n,m}^{(e/h)}(\rho, \varphi) \chi_l^{(e/h)}(z) u_{e/h}, \tag{B1}$$

where $\chi_l^{(e/h)}(z)$ is the wave function for a rigid square well and $u_{e/h} = |j, m_j\rangle$ are the basis functions at the Brillouin-zone center in the Kane model: $|1/2, \pm 1/2\rangle$ and $|3/2, \pm 3/2\rangle$ for the electron and heavy hole, respectively. The planar wave function has the form

$$\begin{aligned}\phi_{n,m}^{(e/h)}(\rho, \varphi) = {} & \frac{1}{\lambda_{(e/h)}} \left(\frac{\Gamma[n + \mathcal{M}_{(e/h)} + 1]}{2^{\mathcal{M}_{(e/h)}} n! \{\Gamma[\mathcal{M}_{(e/h)} + 1]\}^2}\right)^{1/2} \\ & \times \left[\frac{\rho}{\lambda_{(e/h)}}\right]^{\mathcal{M}_{(e/h)}} \frac{e^{-im\varphi}}{\sqrt{2\pi}} e^{-1/4\left[\rho/\lambda_{(e/h)}\right]^2} \\ & \times {}_1F_1 \left\{-n, \mathcal{M}_{(e/h)} + 1, \frac{1}{2}\left[\rho/\lambda_{(e/h)}\right]^2\right\},\end{aligned} \tag{B2}$$

where ${}_1F_1$ is the confluent hypergeometric function, $n = 0, 1, 2, \ldots$ is the radial quantum number, $l = 1, 2, \ldots$ is the vertical quantum number, and $m = 0, \pm 1, \pm 2, \ldots$ labels the angular momentum. The corresponding eigenenergies for the 3D problem are

$$\begin{aligned}E_{n,m,l,s_z}^{(e/h)} = {} & \left[n + \frac{1}{2} + \frac{\mathcal{M}_{(e/h)}}{2}\right] \hbar\omega_{(e/h)} \\ & - \frac{m}{2} \hbar\omega_{c(e/h)}^{*} - \frac{\mu_{(e/h)}^{*}}{4} {\omega_{0(e/h)}}^2 {R_{\rm QR}}^2 \\ & + \left[\frac{l^2\pi^2\hbar^2}{2\mu_{(e/h)}^{*} L^2}\right] + g_{(e/h)}^{*} \mu_B B \cdot s_z,\end{aligned} \tag{B3}$$

with $\mathcal{M}_{(e/h)} = \sqrt{m^2 + 2a_1\mu_{(e/h)}^{*}/\hbar^2}$, $\omega_{c(e/h)}^{*} = eB/\mu_{(e/h)}^{*}$, $\omega_{0(e/h)} = \sqrt{8a_2/\mu_{(e/h)}^{*}}$, $\omega_{(e/h)} = \sqrt{\omega_{c(e/h)}^2 + \omega_{0(e/h)}^2}$ and $\lambda_{(e/h)} = \sqrt{\hbar/\mu_{(e/h)}^{*}\omega_{(e/h)}}$.

APPENDIX C: DETAILS OF THE SOC NONAXISYMMETRIC MODEL

The expression for the spin-orbit Hamiltonian assuming the confinement profile that includes all the asymmetry terms is given by

$$\begin{aligned}H_R^c = {} & 2\alpha_c\sigma_z \left\{\left[-\frac{a_1}{\rho^2} + a_2\rho^2 + \delta\rho^2\cos^2(\varphi)\right]\right. \\ & \left. \times \left(\frac{eB}{2c\hbar} - \frac{i}{\rho^2}\frac{\partial}{\partial\varphi}\right) - i\delta\sin(\varphi)\cos(\varphi)\left(1 + \rho\frac{\partial}{\partial\rho}\right)\right\} \\ & - \alpha_c\frac{\partial V}{\partial z}\left\{\sigma_+\left[e^{-i\varphi}\left(\frac{\partial}{\partial\rho} - \frac{i}{\rho}\frac{\partial}{\partial\varphi} + \frac{eB}{2c\hbar}\rho + \frac{1}{\rho}\right)\right]\right. \\ & \left. -\sigma_-\left[e^{i\varphi}\left(\frac{\partial}{\partial\rho} + \frac{i}{\rho}\frac{\partial}{\partial\varphi} - \frac{eB}{2c\hbar}\rho + \frac{1}{\rho}\right)\right]\right\},\end{aligned} \tag{C1}$$

with $\sigma_{\pm} = 1/2(\sigma_x \pm \sigma_y)$, being σ_i the components of the Pauli matrices. The spin-orbit Hamiltonian for the valence band are readily obtained by replacing these matrices with those for angular momentum $j = 3/2$ and α_c by α_v.

We can extract from Eq. (C1) the diagonal terms that contribute to the first-order renormalization of the spin splitting of the ground state with $m = 0$ for the limit $B \to 0$, $\Delta E_{\text{spin}} = \Delta E^{(0)} + \Delta E^{(1)}$, in the basis of unperturbed states introduced by Eq. (B1). The zero-order value is essentially the Zeeman splitting given by

$$\Delta E_c^{(0)} = g^* \mu_B B, \tag{C2}$$

in the case of the conduction band, while for the valence band stands as

$$\Delta E_v^{(0)} = -6\kappa \mu_B B. \tag{C3}$$

In the case of a conduction-band electron confined within a QD potential, $V = a_2\rho^2 + \delta \times \rho^2 \cos^2\varphi$, the first-order contribution of the spin-orbit interaction, in the limit of low fields, can be reduced to

$$\begin{aligned}\Delta E_c^{(1)} = {} & \frac{4m_0\alpha_c}{\hbar^2} a_2 \\ & \times \left\{1 + \text{sign}(\delta)\frac{e^2}{2 - [1 + \text{sign}(\delta)]\, e^2}\right\} \langle \rho^2 \rangle \mu_B B.\end{aligned} \tag{C4}$$

Meanwhile, for the valence band and a quantum-ring profile, $V = a_1/\rho^2 + a_2\rho^2 - 2\sqrt{a_1 a_2} + \delta \times \rho^2 \cos^2\varphi$, the expression reads

$$\begin{aligned}\Delta E_v^{(1)} = {} & \frac{6m_0\alpha_v}{\hbar^2} \\ & \times \left(a_2 \left\{1 + \text{sign}(\delta)\frac{e^2}{2 - [1 + \text{sign}(\delta)]\, e^2}\right\} \langle \rho^2 \rangle \right. \\ & \left. - a_1 \left\langle \frac{1}{\rho^2} \right\rangle \right) \mu_B B.\end{aligned} \tag{C5}$$

This allows introduction the first-order correction to the Landé factor defined as $g_{c,v}^{(1)} \equiv \Delta E_{c,v}^{(1)}/(\mu_B B)$ and shown in Figs. 9 and 10, respectively. With them, one may now assess the relative effect of the confinement geometry and topology change on the spin splitting. The calculation of the Rashba coefficient appearing in Eq. (C5) is computed from the band parameters in Table I and the expression:

$$\alpha_v = -\frac{eP^2}{3E_0^2} + \frac{eQ^2}{9}\left[\frac{10}{E_0'^2} - \frac{7}{(E_0' + \Delta_0')^2}\right], \tag{C6}$$

which is defined as r_{41}^{8v8v} in [60].

TABLE I. Parameters related with the spin Zeeman effect and band parameters used in the computation of the Rashba coefficient. The values of GaAs and InAs are taken from Ref. [60] (p. 221). The Zeeman parameters of GaSb from Ref. [70] (pp. 486 and 491) and the band parameters from Ref. [71].

	GaAs	InAs	GaSb
g	-0.44	-14.9	-9.25
k	1.20	7.60	4.60
q	0.01	0.39	0.00
E_0 (eV)	1.519	0.418	0.813
E_0' (eV)	4.488	4.390	3.3
Δ_0 (eV)	0.341	0.380	0.750
Δ_0' (eV)	0.171	0.240	0.330
P (eVÅ)	10.493	9.197	9.504
P' (eVÅ)	$4.780i$	$0.873i$	$3.326i$
Q (eVÅ)	8.165	8.331	8.121

APPENDIX D: MATERIAL PARAMETERS

The material band parameters are extracted from [69]. Magnetic related parameters are shown in Table I. The values of the compounds GaInAs and GaAs$_x$Sb$_{1-x}$ are obtained through linear interpolation when no bowing parameter is reported.

[1] P. Michler, ed., *Quantum Dots for Quantum Information Technologies*, Nano-Optics and Nanophotonics (Springer International Publishing, 2017).

[2] S. Nadj-Perge, V. S. Pribiag, J. W. G. van den Berg, K. Zuo, S. R. Plissard, E. P. A. M. Bakkers, S. M. Frolov, and L. P. Kouwenhoven, Spectroscopy of Spin-Orbit Quantum Bits in Indium Antimonide Nanowires, Phys. Rev. Lett. **108**, 166801 (2012).

[3] M. Atatüre, J. Dreiser, A. Badolato, A. Högele, K. Karrai, and A. Imamoglu, Quantum-dot spin-state preparation with near-unity fidelity, Science **312**, 551 (2006).

[4] D. Brunner, B. D. Gerardot, P. A. Dalgarno, G. Wüst, K. Karrai, N. G. Stoltz, P. M. Petroff, and R. J. Warburton, A coherent single-hole spin in a semiconductor, Science **325**, 70 (2009).

[5] M. Vidal, M. V. Durnev, L. Bouet, T. Amand, M. M. Glazov, E. L. Ivchenko, P. Zhou, G. Wang, T. Mano, T. Kuroda, X. Marie, K. Sakoda, and B. Urbaszek, Hyperfine coupling of hole and nuclear spins in symmetric (111)-grown GaAs quantum dots, Phys. Rev. B **94**, 121302 (2016).

[6] K. C. Nowack, F. H. L. Koppens, Y. V. Nazarov, and L. M. K. Vandersypen, Coherent control of a single electron spin with electric fields, Science **318**, 1430 (2007).

[7] J. Pingenot, C. E. Pryor, and M. E. Flatté, Method for full Bloch sphere control of a localized spin via a single electrical gate, Appl. Phys. Lett. **92**, 222502 (2008).

[8] T. Andlauer and P. Vogl, Electrically controllable g tensors in quantum dot molecules, Phys. Rev. B **79**, 045307 (2009).

[9] J. Pingenot, C. E. Pryor, and M. E. Flatté, Electric-field manipulation of the Landé g tensor of a hole in an $\mathrm{In_{0.5}Ga_{0.5}As/GaAs}$ self-assembled quantum dot, Phys. Rev. B **84**, 195403 (2011).

[10] H. M. G. A. Tholen, J. S. Wildmann, A. Rastelli, R. Trotta, C. E. Pryor, E. Zallo, O. G. Schmidt, P. M. Koenraad, and A. Y. Silov, Strain-induced g-factor tuning in single InGaAs/GaAs quantum dots, Phys. Rev. B **94**, 245301 (2016).

[11] F. Klotz, V. Jovanov, J. Kierig, E. C. Clark, D. Rudolph, D. Heiss, M. Bichler, G. Abstreiter, M. S. Brandt, and J. J. Finley, Observation of an electrically tunable exciton g factor in InGaAs/GaAs quantum dots, Appl. Phys. Lett. **96**, 053113 (2010).

[12] V. Jovanov, T. Eissfeller, S. Kapfinger, E. C. Clark, F. Klotz, M. Bichler, J. G. Keizer, P. M. Koenraad, G. Abstreiter, and J. J. Finley, Observation and explanation of strong electrically tunable exciton g factors in composition engineered In(Ga)As quantum dots, Phys. Rev. B **83**, 161303 (2011).

[13] N. Ares, V. N. Golovach, G. Katsaros, M. Stoffel, F. Fournel, L. I. Glazman, O. G. Schmidt, and S. De Franceschi, Nature of Tunable Hole g Factors in Quantum Dots, Phys. Rev. Lett. **110**, 046602 (2013).

[14] P. Corfdir, Y. Fontana, B. Van Hattem, E. Russo-Averchi, M. Heiss, A. Fontcuberta i Morral, and R. T. Phillips, Tuning the g-factor of neutral and charged excitons confined to self-assembled (Al, Ga)As shell quantum dots, Appl. Phys. Lett. **105**, 223111 (2014).

[15] T. M. Godden, J. H. Quilter, A. J. Ramsay, Y. Wu, P. Brereton, I. J. Luxmoore, J. Puebla, A. M. Fox, and M. S. Skolnick, Fast preparation of a single-hole spin in an InAs/GaAs quantum dot in a Voigt-geometry magnetic field, Phys. Rev. B **85**, 155310 (2012).

[16] A. J. Bennett, M. A. Pooley, Y. Cao, N. Sköld, I. Farrer, D. A. Ritchie, and A. J. Shields, Voltage tunability of single-spin states in a quantum dot, Nat. Commun. **4**, 1522 (2013).

[17] J. H. Prechtel, F. Maier, J. Houel, A. V. Kuhlmann, A. Ludwig, A. D. Wieck, D. Loss, and R. J. Warburton, Electrically tunable hole g factor of an optically active quantum dot for fast spin rotations, Phys. Rev. B **91**, 165304 (2015).

[18] V. M. Fomin, ed., *Physics of Quantum Rings* (Springer, Berlin Heidelberg, 2014).

[19] A. Lorke, R. Johannes Luyken, A. O. Govorov, J. P. Kotthaus, J. M. Garcia, and P. M. Petroff, Spectroscopy of Nanoscopic Semiconductor Rings, Phys. Rev. Lett. **84**, 2223 (2000).

[20] A. Fuhrer, K. Ensslin, M. Bichler, S. Lüscher, T. Heinzel, T. Ihn, and W. Wegscheider, Energy spectra of quantum rings, Nature **413**, 822 (2001).

[21] E. Ribeiro, A. O. Govorov, W. Carvalho, and G. Medeiros-Ribeiro, Aharonov-Bohm Signature for Neutral Polarized Excitons in Type-II Quantum Dot Ensembles, Phys. Rev. Lett. **92**, 126402 (2004).

[22] L. G. G. V. Dias da Silva, S. E. Ulloa, and T. V. Shahbazyan, Polarization and Aharonov-Bohm oscillations in quantum-ring magnetoexcitons, Phys. Rev. B **72**, 125327 (2005).

[23] N. A. J. M. Kleemans, I. M. A. Bominaar-Silkens, V. M. Fomin, V. N. Gladilin, D. Granados, A. G. Taboada, J. M. García, P. Offermans, U. Zeitler, P. C. M. Christianen, J. C. Maan, J. T. Devreese, and P. M. Koenraad, Oscillatory Persistent Currents in Self-Assembled Quantum Rings, Phys. Rev. Lett. **99**, 146808 (2007).

[24] I. L. Kuskovsky, W. MacDonald, A. O. Govorov, L. Mourokh, X. Wei, M. C. Tamargo, M. Tadic, and F. M. Peeters, Optical Aharonov-Bohm effect in stacked type-II quantum dots, Phys. Rev. B **76**, 035342 (2007).

[25] I. R. Sellers, V. R. Whiteside, I. L. Kuskovsky, A. O. Govorov, and B. D. McCombe, Aharonov-Bohm Excitons at Elevated Temperatures in Type-II ZnTe/ZnSe Quantum Dots, Phys. Rev. Lett. **100**, 136405 (2008).

[26] M. D. Teodoro, V. L. Campo, Jr., V. Lopez-Richard, E. Marega, Jr., G. E. Marques, Y. Galvão-Gobato, F. Iikawa, M. J. S. P. Brasil, Z. Y. Abu-Waar, V. G. Dorogan, Y. I. Mazur, M. Benamara, and G. J. Salamo, Aharonov-Bohm Interference in Neutral Excitons: Effects of Built-In Electric Fields, Phys. Rev. Lett. **104**, 086401 (2010).

[27] S. Miyamoto, O. Moutanabbir, T. Ishikawa, M. Eto, E. E. Haller, K. Sawano, Y. Shiraki, and K. M. Itoh, Excitonic Aharonov-Bohm effect in isotopically pure $^{70}\mathrm{Ge/Si}$ self-assembled type-II quantum dots, Phys. Rev. B **82**, 073306 (2010).

[28] H. D. Kim, R. Okuyama, K. Kyhm, M. Eto, R. A. Taylor, A. L. Nicolet, M. Potemski, G. Nogues, L. S. Dang, K.-C. Je, J. Kim, J.-H. Kyhm, K. H. Yoen, E. H. Lee, J. Y. Kim, I. K. Han, W. Choi, and J. Song, Observation of a biexciton Wigner molecule by fractional optical Aharonov-Bohm oscillations in a single quantum ring, Nano Lett. **16**, 27 (2016).

[29] Y. Aharonov and D. Bohm, Significance of electromagnetic potentials in the quantum theory, Phys. Rev. **115**, 485 (1959).

[30] A. O. Govorov, S. E. Ulloa, K. Karrai, and R. J. Warburton, Polarized excitons in nanorings and the optical Aharonov-Bohm effect, Phys. Rev. B Rapid Comm. **66**, 081309R (2002).

[31] M. Bayer, M. Korkusinski, P. Hawrylak, T. Gutbrod, M. Michel, and A. Forchel, Optical Detection of the Aharonov-Bohm Effect on a Charged Particle in a Nanoscale Quantum Ring, Phys. Rev. Lett. **90**, 186801 (2003).

[32] R. Okuyama, M. Eto, and H. Hyuga, Optical Aharonov-Bohm effect on Wigner molecules in type-II semiconductor quantum dots, Phys. Rev. B **83**, 195311 (2011).

[33] J. M. Llorens and B. Alén, Wave-function topology effects on charged excitons in type-II InAs/GaAsSb quantum dots and rings, Phys. Status Solidi RRL 1800314 (2018).

[34] J. M. Llorens, L. Wewior, E. R. C. d. Oliveira, J. M. Ulloa, A. D. Utrilla, A. Guzmán, A. Hierro, and B. Alén, Type-II InAs/GaAsSb quantum dots: Highly tunable exciton geometry and topology, Appl. Phys. Lett. **107**, 183101 (2015).

[35] K. Akahane, N. Yamamoto, and N. Ohtani, Long-wavelength light emission from InAs quantum dots covered by GaAsSb grown on GaAs substrates, Phys. E **21**, 295 (2004).

[36] J. M. Ripalda, D. Granados, Y. González, A. M. Sánchez, S. I. Molina, and J. M. Garcia, Room temperature emission at 1.6 μm from InGaAs quantum dots capped with GaAsSb, Appl. Phys. Lett. **87**, 202108 (2005).

[37] H. Y. Liu, M. J. Steer, T. J. Badcock, D. J. Mowbray, M. S. Skolnick, P. Navaretti, K. M. Groom, M. Hopkinson,

and R. A. Hogg, Long-wavelength light emission and lasing from InAs/GaAs quantum dots covered by a GaAsSb strain-reducing layer, Appl. Phys. Lett. **86**, 143108 (2005).

[38] C. Heyn, A. Küster, M. Zocher, and W. Hansen, Field-controlled quantum dot to ring transformation in wave-function tunable cone-shell quantum structures, Phys. Status Solidi RRL 1800245 (2018).

[39] See the Supplemental Material at http://link.aps.org/supplemental/10.1103/PhysRevApplied.11.044011 for the MPL and rate equations details.

[40] J. M. Ulloa, J. M. Llorens, B. Alén, D. F. Reyes, D. L. Sales, D. González, and A. Hierro, High efficient luminescence in type-II GaAsSb-capped InAs quantum dots upon annealing, Appl. Phys. Lett. **101**, 253112 (2012).

[41] M. Hayne and B. Bansal, High-field magneto-photolumine scence of semiconductor nanostructures: High-field magneto-PL of semiconductor nanostructures, Luminescence **27**, 179 (2012).

[42] K. J. Nash, M. S. Skolnick, P. A. Claxton, and J. S. Roberts, Diamagnetism as a probe of exciton localization in quantum wells, Phys. Rev. B **39**, 10943 (1989).

[43] F. Ding, N. Akopian, B. Li, U. Perinetti, A. Govorov, F. M. Peeters, C. C. Bof Bufon, C. Deneke, Y. H. Chen, A. Rastelli, O. G. Schmidt, and V. Zwiller, Gate controlled Aharonov-Bohm-type oscillations from single neutral excitons in quantum rings, Phys. Rev. B **82**, 075309 (2010).

[44] B. Li and F. M. Peeters, Tunable optical Aharonov-Bohm effect in a semiconductor quantum ring, Phys. Rev. B **83**, 115448 (2011).

[45] G. O. de Sousa, D. R. da Costa, A. Chaves, G. A. Farias, and F. M. Peeters, Unusual quantum confined Stark effect and Aharonov-Bohm oscillations in semiconductor quantum rings with anisotropic effective masses, Phys. Rev. B **95**, 205414 (2017).

[46] J. M. Ulloa, R. Gargallo-Caballero, M. Bozkurt, M. del Moral, A. Guzmán, P. M. Koenraad, and A. Hierro, GaAsSb-capped InAs quantum dots: From enlarged quantum dot height to alloy fluctuations, Phys. Rev. B **81**, 165305 (2010).

[47] J. M. Ulloa, J. M. Llorens, M. del Moral, M. Bozkurt, P. M. Koenraad, and A. Hierro, Analysis of the modified optical properties and band structure of $GaAs_{1-x}Sb_x$-capped InAs/GaAs quantum dots, J. Appl. Phys. **112**, 074311 (2012).

[48] P. Klenovský, V. Křápek, D. Munzar, and J. Humlíček, Electronic structure of InAs quantum dots with GaAsSb strain reducing layer: Localization of holes and its effect on the optical properties, Appl. Phys. Lett. **97**, 203107 (2010).

[49] A. Hospodková, M. Zíková, J. Pangrác, J. Oswald, J. Kubištová, K. Kuldová, P. Hazdra, and E. Hulicius, Type I-type II band alignment of a GaAsSb/InAs/GaAs quantum dot heterostructure influenced by dot size and strain-reducing layer composition, J. Phys. D: Appl. Phys. **46**, 095103 (2013).

[50] D. Alonso-Álvarez, B. Alén, J. M. Ripalda, A. Rivera, A. G. Taboada, J. M. Llorens, Y. González, L. González, and F. Briones, Strain driven migration of In during the growth of InAs/GaAs quantum posts, APL Mater. **1**, 022112 (2013).

[51] M. D. Teodoro, A. Malachias, V. Lopes-Oliveira, D. F. Cesar, V. Lopez-Richard, G. E. Marques, E. Marega, M. Benamara, Y. I. Mazur, and G. J. Salamo, In-plane mapping of buried InGaAs quantum rings and hybridization effects on the electronic structure, J. Appl. Phys. **112**, 014319 (2012).

[52] V. Krapek, P. Klenovsky, and T. Sikola, Excitonic fine structure splitting in type-II quantum dots, Phys. Rev. B **92**, 195430 (2015).

[53] W.-C. Tan and J. C. Inkson, Electron states in a two-dimensional ring - an exactly soluble model, Semicond. Sci. Technol. **11**, 1635 (1996).

[54] V. Lopes-Oliveira, Y. I. Mazur, L. D. de Souza, L. A. B. Marçal, J. Wu, M. D. Teodoro, A. Malachias, V. G. Dorogan, M. Benamara, G. G. Tarasov, E. Marega, G. E. Marques, Z. M. Wang, M. Orlita, G. J. Salamo, and V. Lopez-Richard, Structural and magnetic confinement of holes in the spin-polarized emission of coupled quantum ring-quantum dot chains, Phys. Rev. B **90**, 125315 (2014).

[55] V. Lopes-Oliveira, L. K. Castelano, G. E. Marques, S. E. Ulloa, and V. Lopez-Richard, Berry phase and Rashba fields in quantum rings in tilted magnetic field, Phys. Rev. B **92**, 035441 (2015).

[56] M. Sugawara, T. Akiyama, N. Hatori, Y. Nakata, H. Ebe, and H. Ishikawa, Quantum-dot semiconductor optical amplifiers for high-bit-rate signal processing up to 160 Gb s^-1 and a new scheme of 3R regenerators, Meas. Sci. Technol. **13**, 1683 (2002).

[57] L.-W. Yang, Y.-C. Tsai, Y. Li, A. Higo, A. Murayama, S. Samukawa, and O. Voskoboynikov, Tuning of the electron g factor in defect-free GaAs nanodisks, Phys. Rev. B **92**, 245423 (2015).

[58] L. Cabral, F. P. Sabino, V. Lopes-Oliveira, J. L. F. Da Silva, M. P. Lima, G. E. Marques, and V. Lopez-Richard, Interplay between structure asymmetry, defect-induced localization, and spin-orbit interaction in Mn-doped quantumdots, Phys. Rev. B **95**, 205409 (2017).

[59] H. R. Trebin, U. Rössler, and R. Ranvaud, Quantum resonances in the valence bands of zinc-blende semiconductors. I. Theoretical aspects, Phys. Rev. B **20**, 686 (1979).

[60] R. Winkler, *Spin-Orbit Coupling Effects in Two-Dimensional Electron and Hole Systems* (Springer, Berlin Heidelberg, 2003).

[61] J. D. Eshelby, The determination of the elastic field of an ellipsoidal inclusion, and related problems, Proc. R. Soc. Lond. A **241**, 376 (1957).

[62] A. D. Andreev, J. R. Downes, D. A. Faux, and E. P. O'Reilly, Strain distributions in quantum dots of arbitrary shape, J. Appl. Phys. **86**, 297 (1999).

[63] A. Cros, N. Garro, J. M. Llorens, A. García-Cristóbal, A. Cantarero, N. Gogneau, E. Monroy, and B. Daudin, Raman study and theoretical calculations of strain in GaN quantum dot multilayers, Phys. Rev. B **73**, 115313 (2006).

[64] N. Garro, A. Cros, J. M. Llorens, A. García-Cristóbal, A. Cantarero, N. Gogneau, E. Sarigiannidou, E. Monroy, and B. Daudin, Resonant Raman scattering in self-assembled GaN/AlN quantum dots, Phys. Rev. B **74**, 075305 (2006).

[65] D. Jalabert, J. Coraux, H. Renevier, B. Daudin, M.-H. Cho, K. B. Chung, D. W. Moon, J. M. Llorens, N. Garro, A. Cros, and A. García-Cristóbal, Deformation profile in GaN quantum dots: Medium-energy ion scattering experiments and theoretical calculations, Phys. Rev. B **72**, 115301 (2005).

[66] M. Tadić, F. M. Peeters, and K. L. Janssens, Effect of isotropic versus anisotropic elasticity on the electronic structure of cylindrical InP/In$_{0.49}$Ga$_{0.51}$P self-assembled quantum dots, Phys. Rev. B **65**, 165333 (2002).

[67] M. Tadić and F. M. Peeters, Intersublevel magnetoabsorption in the valence band of p-type InAs/GaAs and Ge/Si self-assembled quantum dots, Phys. Rev. B **71**, 125342 (2005).

[68] J. M. Llorens Montolio, PhD thesis, Institut de Ciéncia dels Materials, Universitat de Valéncia, 2007.

[69] I. Vurgaftman, J. Meyer, and L. Ram-Mohan, Band parameters for III-V compound semiconductors and their alloys, J. Appl. Phys. **89**, 5815 (2001).

[70] F. Meier and B. P. Zakharchenya, *Optical Orientation (Modern Problems in Condensed Matter Sciences)* (North-Holland Physics Publishing, Amsterdam, 1984).

[71] M. Cardona, N. E. Christensen, and G. Fasol, Relativistic band structure and spin-orbit splitting of zinc-blende-type semiconductors, Phys. Rev. B **38**, 1806 (1988).